SIMULATION OF SEMICONDUCTOR DEVICES AND PROCESSES Vol. 3
Edited by G. Baccarani, M. Rudan - Bologna (Italy) September 26-28, 1988 - Tecnoprint

Simulation of Non-Planar GaAs Devices

P.J. Haigh, R.E. Miles, C.M. Snowden

Microwave Solid State Group,
Department of Electrical and Electronic Engineering,
University of Leeds,
Leeds, England.

Abstract

A comprehensive numerical simulation has been developed in order to obtain a greater understanding of the operation and limitations of non-planar devices. The simulation employs a new, extremely flexible finite-difference scheme which is capable of fitting a two dimensional mesh to any user defined device domain. The simulation has been used to analyse a coplanar varactor diode, results for which are presented.The model has been extended to investigate the effects of surface states on device performance.

Introduction

The development of monolithic microwave integrated circuits (MMICs) has stimulated particular interest in surface orientated GaAs devices. These devices frequently require intricate, non-planar geometries and complex doping profiles. For example, a coplanar varactor diode has been developed for inclusion in an MMIC oscillator where the topology complements that of the surface orientated GaAs MESFET (*fig. 1*).

The capacitance-voltage characteristics of these devices depend directly on the donor doping profile of the epitaxial layer and in order to obtain a maximum capacitance change, a hyperabrupt doping profile is often used (*fig.* 2). At high bias, the edge of the depletion region is pushed into the low doped region of the epitaxial layer. The sloping sidewall, which is produced by selective etching, was developed to limit the sideways spread of the depletion region at these bias voltages and limit the resulting capacitance change.

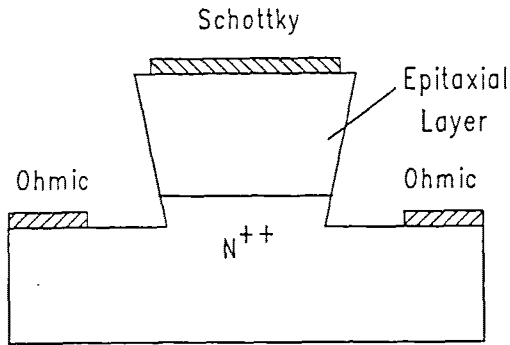

Fig. 1 Coplanar varactor diode

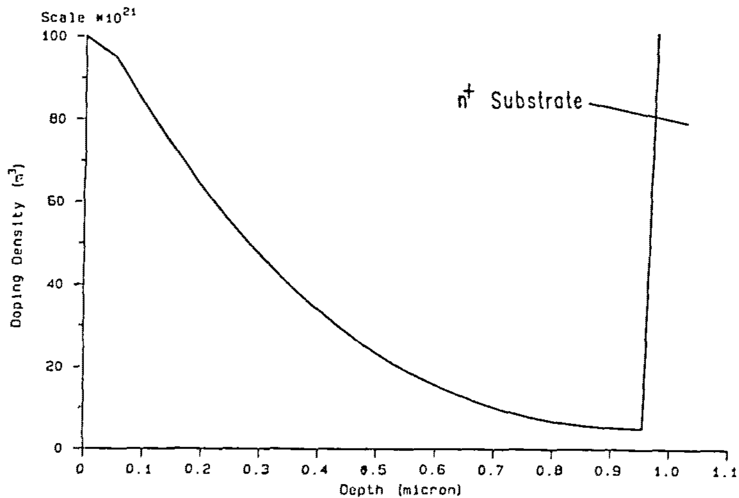

Fig. 2 Doping Profile of A Typical Hyperabrupt Varactor Diode.

The numerical simulation presented here was developed in order to obtain a greater understanding of the physical operation of non-planar GaAs devices such as the coplanar varactor and the model may be used to predict both the D.C., transient and R.F. characteristics. Further, the ability to model arbitrary geometry devices allows the evaluation of complex structures prior to fabrication.

The Classical Semiconductor Equations

The majority of physical device models, where the dimensions of the device geometry are greater than 1 μm employ the classical semiconductor equations. These equations have been derived, both rigorously and heuristically, from the Boltzmann transport equations by several workers, Reiser (1973), Selberherr (1984) and Snowden (1986). In general terms, these models require the self-consistent solution of the following equations[1]

Poisson's equation:

$$\nabla^2\psi = -\frac{q}{\varepsilon_o\varepsilon_r}(N_D - n) \tag{1}$$

where ψ is the electrostatic potential, q is the electronic charge, $\varepsilon_o\varepsilon_r$ is the permittivity, N_D is the donor doping density and n is the electron concentration.

Current continuity:

$$\frac{\partial n}{\partial t} = \frac{1}{q}\nabla.\mathbf{J}_n + G \tag{2}$$

where J_n is the electron density and G is the generation-recombination rate, which in most unipolar devices such as MESFETs and Schottky varactor diodes is assumed to be negligible for normal operating conditions.

Current density:

$$\mathbf{J}_n = qn\mathbf{v}_n + qD_n\nabla n \tag{3}$$

where $\mathbf{v}_n$ is the electron drift velocity and D_n is the electron diffusion coefficient.

The diffusion coefficient, D_n, is often defined in terms of the Einstein relationship.

$$D_n = \frac{kT}{q}.\mu_n \tag{4}$$

where k is the Boltzmann constant and T is the lattice temperature. Frequently, the drift velocity term in equation (4) is replaced by:

$$\mathbf{v}_n = -\mu_n\mathbf{E} \tag{5}$$

where, the electric field

$$\mathbf{E} = -\nabla\psi \tag{6}$$

The current, I associated with the contact of the semiconductor device is obtained by intergrating the total current density, J across a suitable surface surrounding the contact.

$$I = \int_s \mathbf{J}.ds \tag{7}$$

The total current density, **J** includes both the particle current, $\mathbf{J}_n$ and the displacement current

$$\mathbf{J} = \mathbf{J}_n + \varepsilon_r\varepsilon_o\frac{\partial \mathbf{E}}{\partial t} \tag{8}$$

[1] Unipolar devices such as MESFETs and Schottky varactor diodes are usually analysed using a single species set of the basic transport equationsowever, the treatment for holes is entirely analogous.

The physical model described by these equations is subject to three main assumptions. These are that the carrier velocities respond instantaneously to changes in the electric field and that the mobility and diffusion coefficients are functions of the electric field alone. In practice, this seems to be an adequate approximation in circumstances where the electric field is changing slowly with time and space. The mobility and diffusion coefficients are dependent on several parameters (for example electron temperature, carrier concentration and electric field) (Doades,1984, Snowden,1986). The influence of hot electron effects in smaller geometry devices is discussed elsewhere (for example, Snowden, 1987).

Modelling of the boundary conditions

The domain of the device model is defined by the geometry chosen to represent the actual device. The surface orientated nature of non-planar devices requires a two dimensional model to account for the non-uniform nature of the electric field and electron distribution. The boundary of the simulation domain consists of two components; real "physical" boundaries such as contacts and free surfaces and internal boundaries which limit the device domain within the semiconductor.

Schottky Contacts

The simulation incorporates a sophisticated Schottky contact model which is capable of modelling accurately both thermionic and thermionic-field emissions.

The J_{TE} component is expressed in terms of an effective recombination velocity, ν_r and a quasi-equilibrium electron density n_o.

$$J_{TE} = q(n_s - n_o)\nu_r \tag{9}$$

where n_s is the electron concentration on the semiconductor side of the Schottky contact. The effective recombination velocity is given by (Sze,1981).

$$\nu_r = \frac{A^* T^2}{qN_c} \tag{10}$$

where A^* is the effective Richardson constant and N_c is the effective density of states in the conduction band (Sze,1981). The quasi-equilibrium electron density is obtained from

$$n_o = N_c.\exp\left[-q\frac{\phi_{bn}}{kT}\right] \tag{11}$$

where $q\phi_{bn}$ is the barrier height and k is the Boltzmann constant. The potential ψ_s at the Schottky barrier interface is

$$\psi_s = V_A - \phi_{bn} \tag{12}$$

where V_A is the applied potential on the Schottky metalisation.

Analysis of the thermionic-field component, J_{TFE} is more complicated, since the shape of theotential barrier (hence the doping profile)

affects the tunnelling current-voltage characteristic. Analytical expressions for the reverse bias I-V characteristic in the case of hyperabrupt profiled Schottky barriers have been developed by Tasker (1983) by re-writing the obtained by Padovani and Stratton (1966) in terms of the maximum electric field at the interface, ξ_m.

$$J_{TFE} = J_s \exp\left[\left(\frac{\xi_m}{\xi_o}\right)^2\right] \quad (13)$$

where

$$J_s = \frac{A^* T^2 (\pi E_{oo})^{1/2}}{kT} \left[\frac{q^2 \xi_m^2}{E_{oo}^2 \alpha^2} - q\phi_b \tanh^2\left(\frac{E_{oo}}{kT}\right)\right]^{1/2} \exp\left[-\frac{q\phi_{bn}}{kT}\right] \quad (14)$$

$$\xi_o = E_{oo}^{\frac{3}{2}} \alpha \left[\frac{E_{oo}}{kT} - \tanh\left(\frac{E_{oo}}{kT}\right)\right]^{-1/2} \quad (15)$$

$$E_{oo} = \frac{2q}{\alpha}\left(\frac{N_D}{2\varepsilon_s}\right)^{1/2} \quad (16)$$

and

$$\alpha = \frac{2}{\hbar}(2m_s^*)^{1/2} \quad (17)$$

The total electron current density through the contact is given by the sum of the thermionic emission and thermionic-field emission components, i.e.

$$J_{TOT} = J_{TE} + J_{TFE} \quad (18)$$

Surfaces

The influence of surface charge and passivation can significantly effect the physical operation of small geometry devices. The surface conditions are invariably modelled using Neumann boundary conditions and may be expressed as

$$\frac{\delta\psi}{\delta\vec{n}} = \frac{Q_{surf}}{\varepsilon_s} \quad (19)$$

where Q_{surf} is the charge on the surface of the semiconductor which is given by

$$Q_{surf} = qD_s \quad (20)$$

where D_s is the density of surface states.

In the absence of more reliable data, the density of occupied surface states is usually assumed constant at $10^{16}\ m^{-2}.eV^{-1}$ at a doping density of $10^{23} m^{-3}$ (Williams, 1983). Although satisfactory in high doped regions, this approach results in very long space-charge regions in areas of low doping density. Consequently, this technique was not suitable for inclusion in

this simulation where the doping density may be as low as 10^{21}. On n-type GaAs surfaces, the surface states pin the Fermi level at the surface at around $E_c - 0.8$ eV. Therefore, a more realistic surface state model was implemented by pinning the potential at "exterior" nodes which are very close to the surface of the device. The effects of surface depletion on device performance are analysed later in this paper.

Internal boundaries must be introduced in order to limit the device domain. However, *a priori* knowledge of the symmetry and operation of the device usually allows the definition of suitable boundaries. These surfaces are modelled using Neumann boundary conditions and it is assumed that the potential and carrier gradients normal to the surface are zero,

$$\frac{\delta\psi}{\delta\vec{n}} = 0, \quad \frac{\delta n}{\delta\vec{n}} = 0 \tag{21}$$

Implementation

The software generates a finite-difference mesh automatically at run-time using data supplied interactively by the operator. As well as fitting a suitable mesh to a complex arbitrary device domain, the program is sufficiently flexible to undertake automatic mesh refinement, incorporating the technique of finite boxes (Franz *et al*,1983), as required.

The initial mesh used in the simulation of the coplanar varactor diode is shown in *fig. 3*. Once the mesh has been created, using a similar technique to that described by Barton (1986), the horizontal mesh lines are sorted by y coordinate and the domain can then be traversed in an efficient manner. Note that only half the device is analysed as the coplanar varactor is both electrically and physically symmetrical about the centre of the Schottky contact.

Discretisation of the Semiconductor Device Equations

The finite-difference equations used in this work are derived from second-order truncated Taylor series expansions for the semiconductor device equations and assume the these equations are single valued with continuous derivatives. This form of discretisation is very well documented (Reiser,1973; Selberherr,1984; Snowden,1986) and usually employs the classical five point difference scheme in which a central node is surrounded by four neighbours (*fig. 4*). The discretisation of the parabolic current continuity equation is considerably more difficult than that of the elliptic Poisson equation due to the time dependence. In order to minimise the discretisation error, the current density is calculated at the half points surrounding the central node. Localised mesh refinement may be implemented using the technique of Franz *et al* (1983) which results in a six point discretisation. (*fig. 4*).

Discretisation of the boundary conditions

Dirichlet boundary conditions, where the potential and carrier concentrations are fixed at some pre-defined value, are easily implemented using finite-differences and are frequently used to model Ohmic contacts. As previously stated, contact-free surfaces are usually modelled using

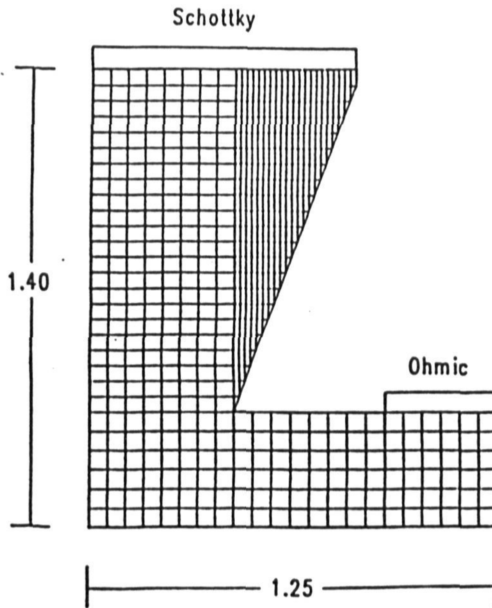

Fig. 3 Initial mesh used in the simulation of the coplanar diode.

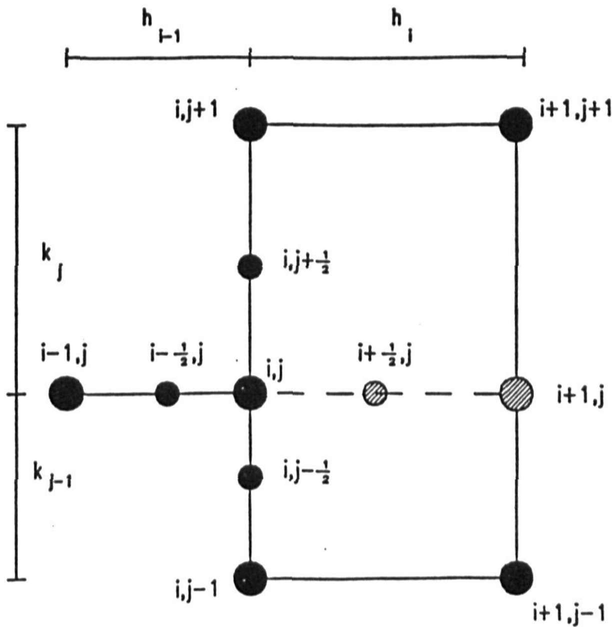

Fig. 4 Five point discretisation and extended six point scheme.

Neumann boundary conditions the implementation of which can be rather complex, particularly in the transition between Neumann and Dirichlet boundaries and on surfaces which are not orthogonal to the coordinate axes. The discretised approximations to the derivative boundary conditions may be formulated in several ways. The most popular methods employ either the Newton polynomial or the central difference formula (sometimes referred to in this context as the Stirling polynomial). It is the latter technique which has been implemented in this simulation as it offers improved accuracy, particularly in regions where the solution is rapidly changing.

Considering the situation at a bevelled boundary (*fig. 5*); the boundary condition for derivatives perpendicular to the device surface may be expressed as (Franz *et al*,1983)

$$\frac{\partial\psi}{\partial\vec{n}} = \frac{\partial\psi}{\partial x}\cos\theta + \frac{\partial\psi}{\partial y}\sin\theta \qquad (22)$$

where $\vec{n}$ is the normal to the surface and θ is the angle between the perpendicular and the bevelled edge.

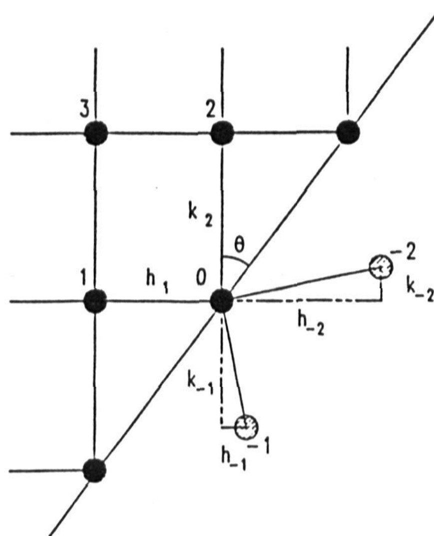

Fig. 5 Boundary Conditions for Bevelled Surface.

Although a step model for the bevelled surface was considered, this technique was rejected as such a surface would be extremely susceptible to singularities occurring at the re-entrant corners. Consequently, a novel, second order difference scheme was developed requiring the introduction of two "exterior" nodes, -1, -2, which are the reflection of the nodes 1, 2 about the bevelled surface.

In order to approximate the Laplacian operator, $\nabla^2\psi_0$, it is assumed that (Greenspan,1965)

$$\nabla^2\psi_0 = \sum_{i=-1}^{2} \alpha_i\psi_i \qquad (23)$$

If Taylor series expansions for ψ_{-2}, ψ_{-1}, ψ_1, ψ_2, ψ_3 are performed about the point numbered 0 and substituted into equation (23), then the Laplacian operator may be expressed as

$$\begin{aligned}
\nabla^2\psi_0 \equiv\ & \psi_0(\alpha_{-2} + \alpha_{-1} + \alpha_0 + \alpha_1 + \alpha_2 + \alpha_3) \\
& + \frac{\partial\psi_0}{\partial x}\left(\alpha_{-2}h_{-2} + \alpha_{-1}h_{-1} - \alpha_1 h_1 - \alpha_3 h_1\right) \\
& + \frac{\partial\psi_0}{\partial y}\left(\alpha_{-2}k_{-2} - \alpha_{-1}k_{-1} + \alpha_2 k_2 + \alpha_3 k_2\right) \\
& + \frac{1}{2}\left[\frac{\partial^2\psi_0}{\partial x^2}\left(\alpha_{-2}(h_{-2}^2) + \alpha_{-1}(h_{-1}^2) + \alpha_1(h_1^2) - \alpha_3(h_1^2)\right)\right] \\
& + \frac{\partial^2\psi_0}{\partial x\partial y}\left(\alpha_{-2}(h_{-2}k_{-2}) - \alpha_{-1}(h_{-1}k_{-1}) + \alpha_3(h_1 k_2)\right) \\
& + \frac{1}{2}\left[\frac{\partial^2\psi_0}{\partial y^2}\left(\alpha_{-2}(k_{-2}^2) + \alpha_{-1}(k_{-1}^2) + \alpha_2(k_2^2) + \alpha_3(k_2^2)\right)\right]. \\
& + O\left(max\,(h_i, k_i)^2\right)
\end{aligned} \qquad (24)$$

The α_i's may be determined from this system of equations by employing Gaussian-Elimination and partial pivoting with back substitution. Although the calculation of the α_i's, the "distance factors", appears complex, they are only dependent on the inter-node distances and the angle, θ, of the bevelled surface.

The ability to model accurately bevelled and multi-bevelled surfaces is well within the scope of this technique as the nodes surrounding the central node may assume arbitrary positions. Furthermore, it may be shown that the six point formula (Franz *et al*,1983) is merely a special case of this general six point scheme (24).

Solution of the Discretised Device Equations

The discretisation of the semiconductor device equations yields large systems of simultaneous equations with sparse coefficient matrices which are ideally suited to iterative solution methods (Snowden,1986). The discretised Poisson equation is rearranged to give $\psi_{i,j}$ in terms of the potential at the surrounding nodes and is solved using successive over relaxation (SOR). The current continuity equation is solved in a similar manner, but in this case the relaxation parameter ω lies in the range $0 < \omega \leq 1$, a technique known as successive under relaxation (SUR). This process is repeated until the solution converges. A flowchart of the complete simulation procedure is presented in *fig. 6*.

In order to guarantee convergence, these solution techniques require diagonally dominant or positive definite matrices. One drawback of the new boundary conditions is that the resulting system of equations is structurally unsymmetric. However, convergence using relaxation methods is usually possible although the optimum relaxation parameter ω must be

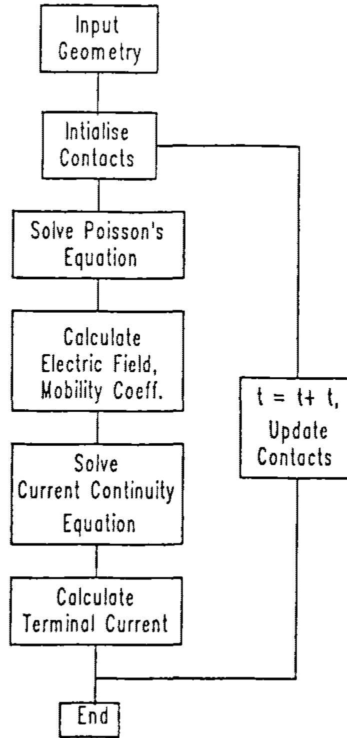

Fig. 6 Flowchart of Device Simulation.

determined empirically as this factor is dependent on the shape of the device domain.

Simulation Results

Contour plots of potential and electron density for the coplanar hyperabrupt varactor diode (*fig. 3*) are shown in *fig. 7*. The doping profile employed is that shown in *fig. 2* and the Schottky contact is biased at $-3\,V$. The depleted region under the Schottky contact is clearly visible and the crowding of the potential contours around the contact indicates the extremely high electric fields present. The surface state model pins the exterior surface potential at around $-0.8\,V$ and the plots highlight the non-linear nature of the surface depletion due to the complex, hyperabrupt doping profile.

An investigation into the effects of surface states was undertaken and *fig. 8* shows the C-V profile of the coplanar varactor with and without the surface state model. The marked difference in the two characteristics emphasises the importance of modelling accurately the device boundary conditions.

A large signal r.f. analysis was performed at $10\,GHz$ (*fig. 9*). A sinusoidal r.f. voltage was imposed (at $-4\,V$ D.C. bias) and the

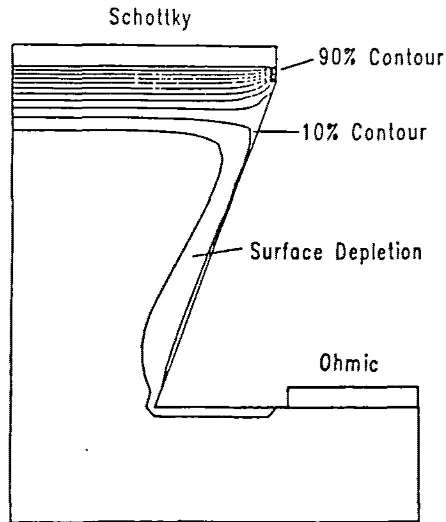

Fig. 7a Contour plot of potential for the coplanar varactor diode.

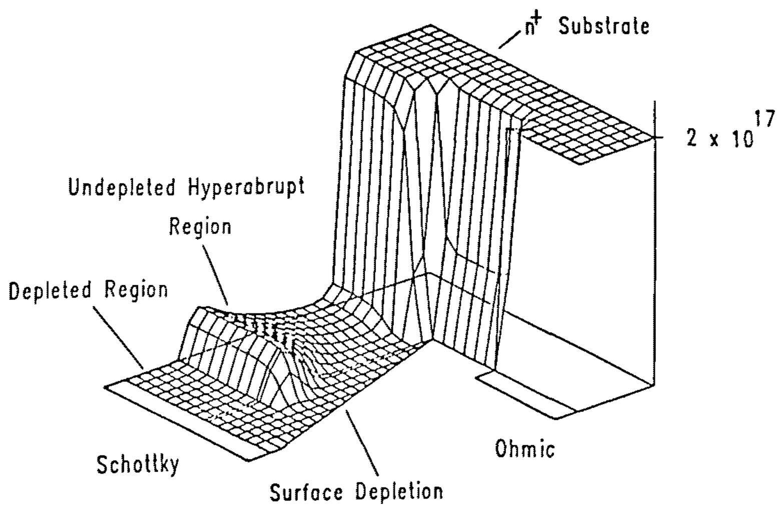

Fig. 7b Isometric plot of electron density for the coplanar varactor diode.

corresponding current values were calculated at each time step. A harmonic analysis of these waveforms allows the calculation of the device impedance.

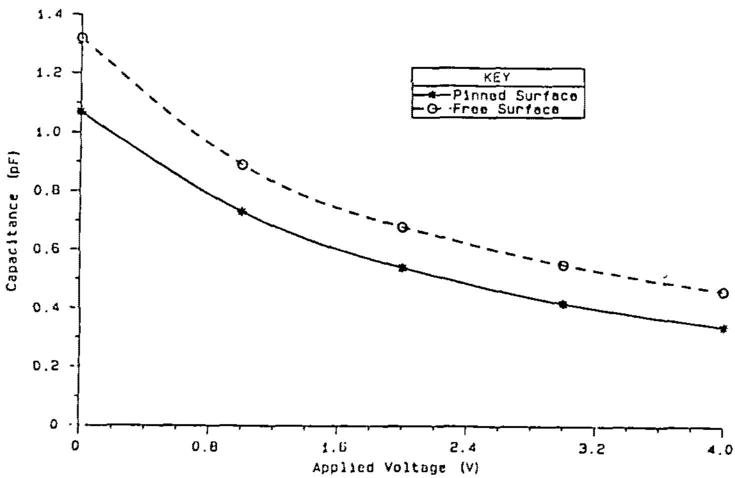

Fig. 8 Effect of surface states on C-V characteristic of the coplanar diode.

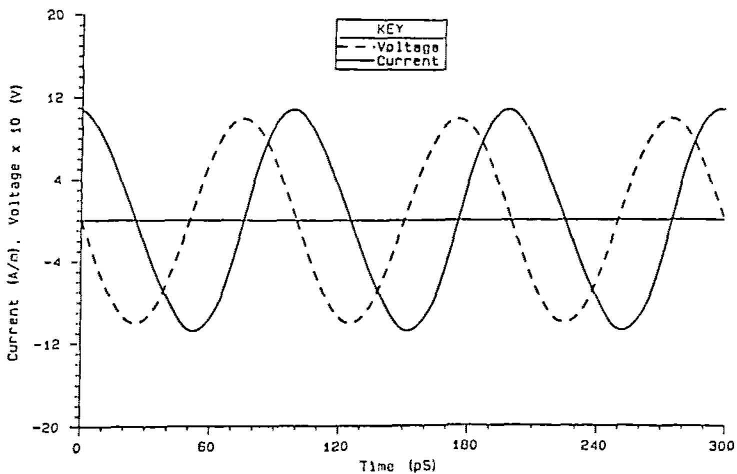

Fig. 9 R.F. Current and voltage waveforms.

In order to validate the simulation, the C-V characteristics of several abrupt junction CXY23 (Philips Microwave) series diodes have been determined and a comparison with simulated results is presented in *fig. 10.*

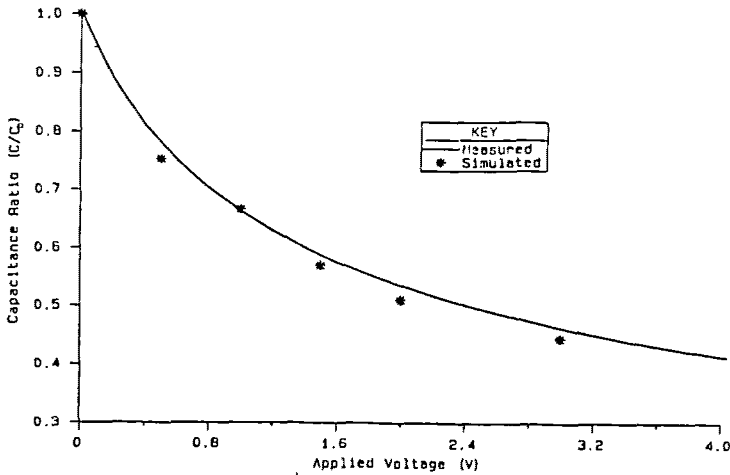

Fig. 10 Comparison of measured and simulated results.

Conclusion

The modified finite-difference scheme presented here is capable of modelling non-planar GaAs devices with complex doping profiles. A new extremely flexible six point scheme has been developed which allows a two-dimensional discretisation mesh to be fitted to any user defined device domain. The investigation into the effects of surface states on device performance has highlighted the importance of considering these effects when designing small geometry devices. Analysis of the D.C. and R.F. characteristics predicted by the simulation allows the optimisation of the geometry and doping profile of the coplanar varactor. Work into the validation of the simulation is continuing by comparing both measured and simulated results (both R.F. and D.C.) from several non-planar devices.

Acknowledgements

The authors wish to acknowledge the support of Philips Microwave and the SERC.

REFERENCES

Barton T.M., Snowden C.M., Richardson J.R. (1986),
"Modelling of Recessed Gate MESFET Structures", *2nd Int. Conf. on Simulation of Semiconductor Devices and Processes*, Swansea, Pineridge Press pp 528-543.

Doades G.P., Howes M.J., Morgan D.V., (1984),
"Performance of GaAs Device Simulations at Microwave Frequencies", *Int. Conf. on Simulation of Semiconductor Devices and Processes*, Swansea: Pineridge Press, pp 353-367.

Franz A., Franz G., Selberherr S., Ringhofer C., Markowich P. (1983),
"Finite Boxes - A Generalisation of the Finite-Difference Method Suitable for Semiconductor Device Simulation", *IEEE Trans. Electron Devices, ED-30*, pp 1070-1082.

Greenspan D. (1965),
Introductory Numerical Analysis of Elliptic Boundary Value Problems", Harper and Row.

Padovani F. A. and Stratton R. (1966),
"Field and Thermionic-Field Emission in Schottky Barriers", *Solid-State Electron., Vol 9*, pp 695-707.

Reiser M. (1973),
"A Two-Dimensional Numerical FET Model for DC, AC and Large-Signal Analysis", *IEEE Trans. Electron Devices, ED-20*, pp 35-45.

Selberherr S. (1984),
Analysis and Simulation of Semiconductor Devices, Springer-Verlag, Austria.

Snowden C. M. (1986),
Introduction to Semiconductor Modelling, World Scientific.

Snowden C.M. and Loret D. (1987),
"Two-Dimensional Hot-Electron Models for Short-Gate-Length GaAs MESFETs", *IEEE Trans. Electron Devices, ED-34* pp 212-223.

Sze S. M. (1981),
Physics of Semiconductor Devices, John Wiley and Sons.

Tasker P.J. (1983),
"Ion Implanted GaAs Hyperabrupt Varactor Diodes", *PhD. Thesis*, University of Leeds.

Williams R. H. (1983),
"Semiconductor Surfaces and Interfaces", *Vacuum, Vol. 33*, Nos 10-12, pp 587-592.

SIMULATION OF SEMICONDUCTOR DEVICES AND PROCESSES Vol. 3
Edited by G. Baccarani, M. Rudan - Bologna (Italy) September 26-28, 1988 - Tecnoprint

NEAR BALLISTIC TRANSPORTS IN SWITCHING OPERATIONS OF GaAs MESFET'S WITH A SUBMICROMETER GATE-LENGTH OBSERVED BY MULTI-PARTICLE SIMULATION

Y. Yamada, N. Shimojoh

Department of Electrical Engineering and Computer Sciences
Kumamoto University, Kumamoto 860, Japan

SUMMARY

Here we study near ballistic transports proper to switching operations of GaAs MESFET's with a 0.5 μm gate-length, using a multi-particle simulator. The time-resolved distributions of electron velocity, electron energy, electric-field and carrier density along the channel related with ON↔OFF operations are obtained, in addition to time responses of the currents. The near ballistic transports proper to the ON↔OFF operations are significant near the source electrode and underneath the gate. The dynamics of the particles in upper valleys which determines the switching time is depicted. It is tried to evaluate the relaxation times of momentum and energy both from their time responses and from the steady state distributions of velocity, energy and so on. It is found that the well-known ballance equations of momentum and energy underestimates electron energy and overestimates electron velocity underneath the gate.

INTRODUCTION

Recently a multi-particle simulator, which can exactly take into account near ballistic transports in submicrometer gate GaAs MESFETs, has been widely applied to evaluation of the characteristics. However few reports have been published on details of electron dynamics in switching operations, although there is only a few papers on calculation of a time response of the drain current and a switching time, which were reported by Yoshii, Tomizawa, and Yokoyama(1983), and Yokoyama, Tomizawa, and Yoshii(1985). It is necessary to publish the details of electron dynamics for modelling and further development of a more tractable method such as relaxation time approximation, which are proposed or simplified by Blotekjaer(1970), Cook and Frey(1982), and Stenzel, Elschner, and Spallek(1987). The relaxation time approximation will be applied to CAD of the

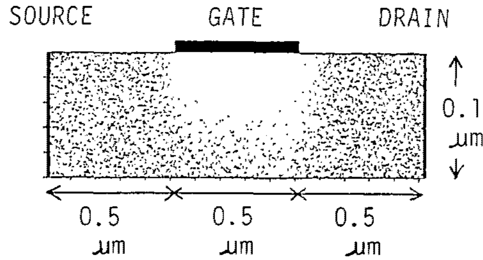

Fig. 1. Schematic drawing of a MESFET device used in the simulation. The small dots denote particles.

device in the near future, because it does not require big computer resources and is able to carry out time-resolved calculation without any numerical noise, in contrast to the multi-particle simulator.

In the present paper, in addition to the time responses of the currents, electron dynamics in the switching operations, such as velocity, energy, electric-field, and carrier density, will be depicted in detail. Next the same technique will be applied to observation of relaxation processes of energy and momentum at some points in the device. Finally accuracy of the relaxation time approximation will be discussed through the relaxation times.

MULTI-PARTICLE SIMULATOR

The multi-particle simulator has been applied to the device shown in fig. 1. The doping density of donor is 10^{17} cm^{-3} and lattice temperature is 300 K. The electric-field in the device is self-consistently calculated with the particle distribution through Poisson's equation. The Monte Carlo technique used in the present simulation is followed by Fawcett, Boardman, and Swain(1970). Their model for the conduction band is a two-valley one. The number of particles in the device is 10,000 at the initial step of the simulation. Figure 1 shows a steady state distribution of particles in a ON state which are denoted by small dots.

NEAR BALLISTIC TRANSPORTS IN SWITCHING OPERATIONS

Figure 2 shows a scheme of the switching operation of the gate voltage(V_G) and the corresponding time-responses of the source current(I_S) and the drain current(I_D). The drain voltage (V_D) is 1.0 V. The currents consist of drift and displacement currents. The drift component is dominant at the source and drain, while the displacement component is dominant at the gate. The multi-particle simulator causes large numerical noise in the calculated results, especially in the transient data. In addition, the currents at the source, gate, and drain electrodes are not instantaneously ballanced due to the numerical noise. However we can find out features of the transports during the

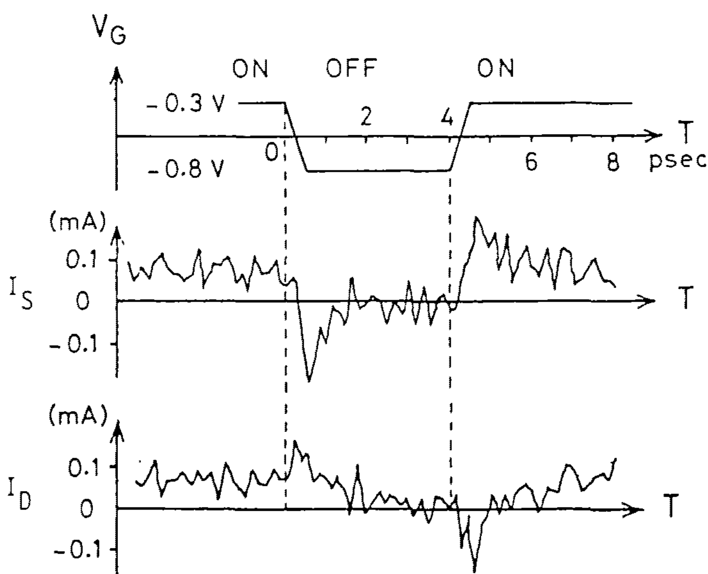

Fig. 2. A scheme of switching operation and the time responses of the source current(I_S) and drain current(I_D).

switching operations. The switching time in fig. 2 is 3-4 psec. The figures from fig. 3 to fig. 8 show the time-resolved distributions of velocity, energy, electric-field, and carrier density just after the switching near the bottom of the channel. Here the velocity and electric-field are parallel to the channel.

First let us observe the transports during the ON → OFF operation. For time less than 1 psec, the particles in a lower valley in the source side underneath the gate ballistically move toward the source due to the negative field more than -10 kV/cm, but they do not change into upper valleys, as shown in figs. 3 (b) and 3(e), due to the rather small amplitude of V_G. Their velocity exceeds $4x10^7$ cm/s instantaneously, which is close to the maximum velocity of the ON steady state. In the drain side there are many particles in the upper valleys in the ON steady state. They do not almost change their behaviours during the small period in spite of large change of the electric-field there, because their effective mass is very large. It takes more than 3 psec for them to be cooled in to a lower valley. The undershoot and overshoot in the time responses of I_S and I_D, respectively, and the slow variation of I_D just after the overshoot reflect the above transports.

Next let us see the transports during the OFF → ON operation. We observe two kinds of near ballistic transports near the source electrode and underneath the gate. The one occurcs at about 4.44 psec near the source electrode due to the electric-field of about 6 kV/cm shown in fig. 5. This transport is shown in the enlarged figure of fig. 6. The accelerated particles are

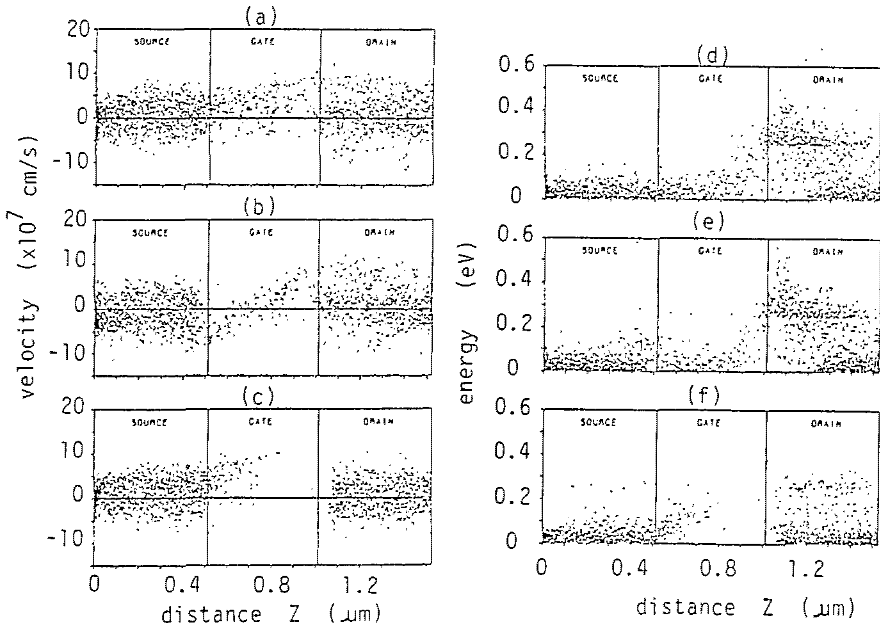

Fig. 3. The distributions of particle velocity parallel to the channel and particle energy in the ON steady state((a), (d)), at 0.73 psec((b),(e)), and at 4.70 psec((c),(f)).

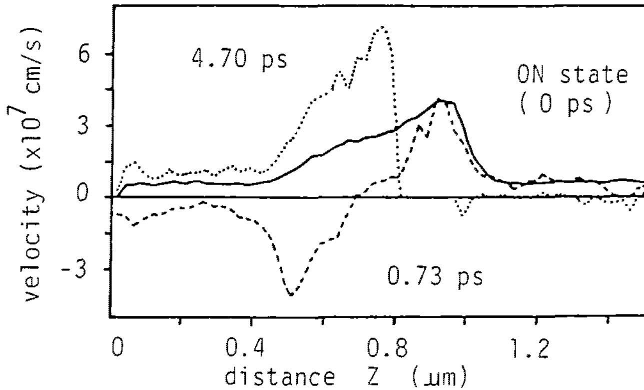

Fig. 4. The distributions of average velocity parallel to the channel along the bottom of the channel in the ON steady state, at 0.73 psec, and at 4.70 psec.

not perfectly cooled at the source side under the gate. The another near ballistic transport starts after about 4.4 psec under the gate. The particles in the lower valley which reach the source side under the gate are again accelerated by the electric-field of about 12 kV/cm shown in fig. 5 and move toward the drain ballistically. Their velocity reaches about 7×10^{17} cm/s as shown in fig. 4, which is fairly larger than the

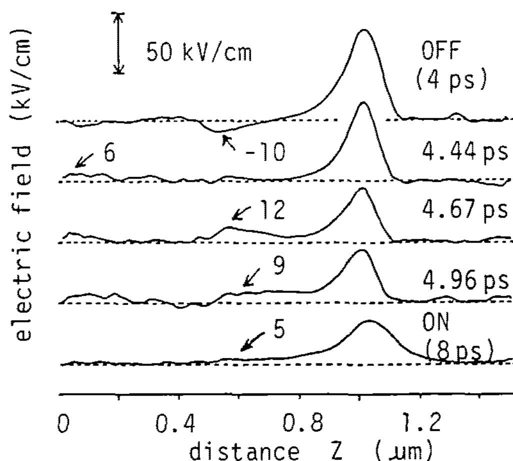

Fig. 5. The time-resolved distributions of electric-field parallel to the channel along the bottom of the channel in the OFF state(4 psec), at 4.44 psec, at 4.67 psec, at 4.96 psec, and in the ON state(8 psec).

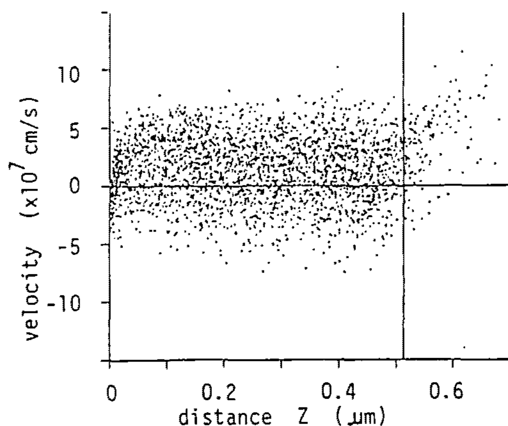

Fig. 6. The distribution of particle velocity parallel to the channel near the source electrode. The velocities of particles sharply rise in the neighbourhood of the source electrode and relax hereafter.

maximum velocity of the ON state. This accelerating electric-field decreases as the number of particles coming into the region under the gate increases. After about 5.5 psec the fastest particles reach the drain edge of the channel under the gate. Most of these particles are scattered into upper valleys due to inter-valley scatterings. First the generation of the particles in the upper valleys occures at the bottom of the

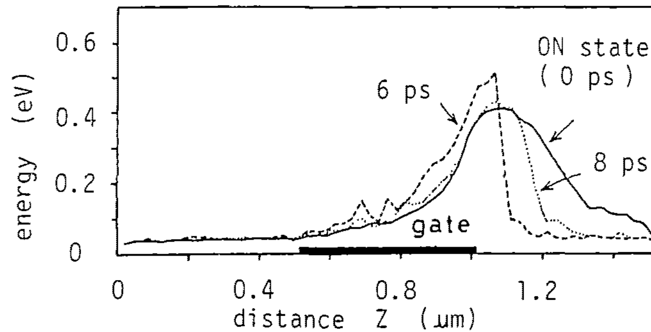

Fig. 7. The time-resolved distributions of average energy along the bottom of the channel at 6 psec, at 8 psec, and in the ON steady state during the OFF → ON operation.

channel and then the particles slowly drift toward the drain and upward due to their large effective mass. Finally they are cooled into the lower valley as they come close to the drain electrode. It takes more than 4 psec for their distribution of energy to reach the steady state one, as shown in fig. 7. Thus, the transports described above are cleary reflected in the overshoot and undershoot of I_S and I_D, respectively, and the slow variation of I_D just after the undershoot.

Thus, the slow responses of I_D just after the overshoot and undershoot are responsible for the slow movements of the particles in the upper valleys. Perhaps the responses may depend on V_D, because the population of the upper valleys

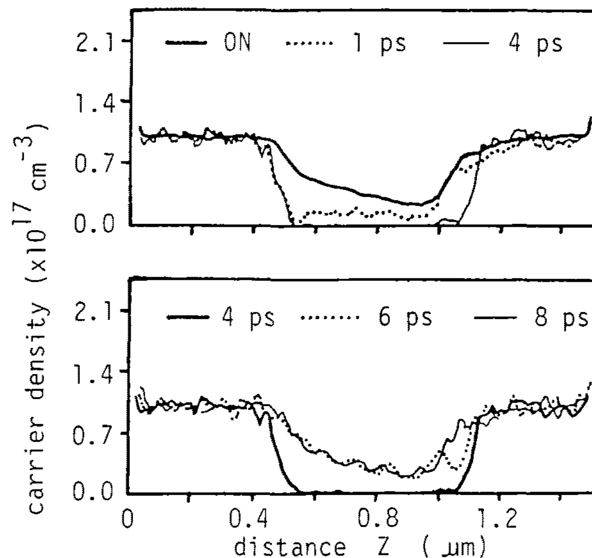

Fig. 8. The time-resolved distributions of carrier density along the bottom of the channel in a sequence of the ON → OFF → ON operation.

increases with V_D.

Figure 8 shows the time-resolved distributions of carrier density along the bottom of the channel. In the ON → OFF switching, the particles in the middle of the channel under the gate do not quickly move due to the almost zero electric-field there. In the OFF → ON switching, the particles temporary accumulate at the drain edge of the channel under the gate due to intervalley scattering, as shown by the dotted line, because there are no particles under the gate in the OFF state, and the accumulation vanishes as the many particles in the upper valleys drift toward the drain.

RELAXATION OF ENERGY AND MOMENTUM IN THE DEVICE

Next we have simulated the relaxation of energy and momentum in the device. In this simulation, the drain voltage is changed suddenly from 1.0 V(ON state) to zero. The gate voltage remains constant(-0.3 V) during the simulation.

Figures 9(a)-9(d) show the time-resolved distributions of the carrier density, electric field, momentum and energy along the bottom of the channel. The electric-field and momentum are parallel to the channel. The carrier density, electric-field, and momentum quickly relax within 0.7 psec, while the energy slowly relaxes.

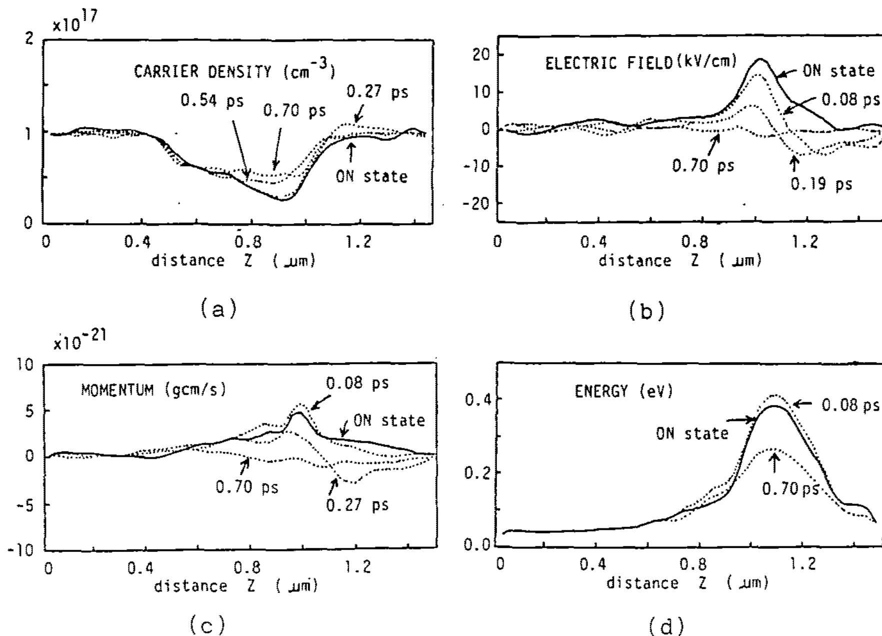

Fig. 9. The time-resolved distributions of carrier density(a), electric-field(b) and momentum(c) parallel to the channel, and energy(d) in the relaxation.

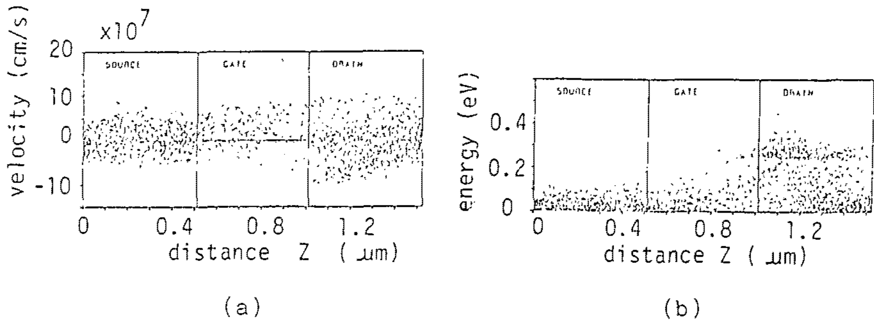

Fig. 10. The distributions of particle velocity(a) and energy (b) at 0.22 psec after the switching. The velocity is parallel to the channel.

Figures 10(a) and 10(b) show the distributions of velocity and energy of all the particles in the device, respectively, at 0.22 psec after the switching. The velocity is parallel to the channel. The particles in the lower valley near the drain drift backward by the negative field ballistically. The instantaneous increase of the energy shown in fig. 9(d) is caused by this particle behaviour. On the other hand the particles in the upper valleys hardly change their behaviour in this period.

Figure 11(a) shows the time responses of momentum at three points in the device which are denoted by the solid lines. Their energies just before the switching are listed in the figure. Although the carrier density and the energy vary somewhat in this period, we have estimated the time constants for fig. 11(a) taking into account variation of the electric-field only. The time constants are shown by the closed circles in fig.12. They are smaller than the relaxation time of momentum(τ_p) obtained from steady state data by an ensemble Monte carlo simulation for an uniform electric-field case. The τ_p is shown by the dotted line in fig. 12. Figure 11(b) shows the time responses of energy and population of the lower valley. The time responses at two points with the almost same energy in the ON state are shown together in the figure. As it is considered that the variations of the carrier density and the electric-field almost vanish within about 0.70 psec after the switching, we have simply considered that the time constants in fig. 11(b) correspond to the relaxation time of energy. The open circles in fig. 12 show the time constants. They qualitatively agree with the solid line which are the relaxation time of energy(τ_ε) obtained from the same method as the dotted line.

We have shown the time-resolved distributions of the carrier density, the electric-field, the momentum and the energy in the relaxation. The present results may be useful for discussion about accuracy of the relaxation time approximation cited in INTRODUCTION.

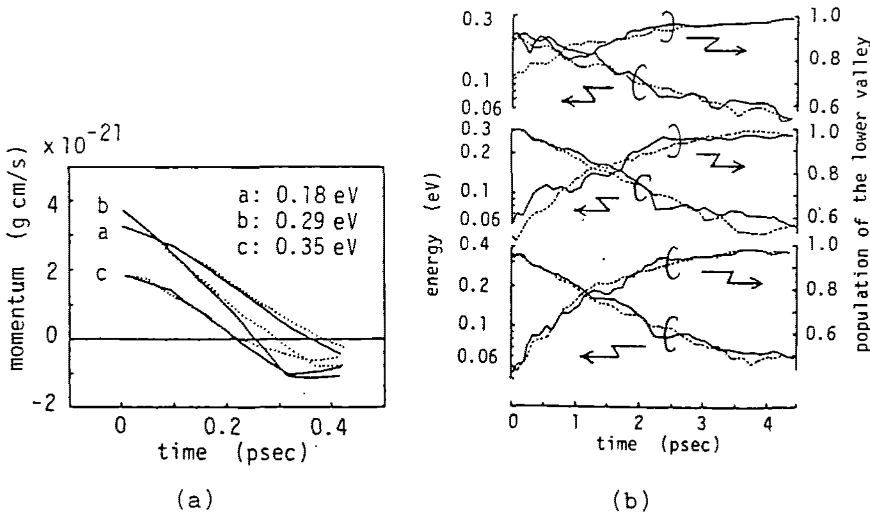

Fig. 11. (a) The time responses of momentum parallel to the channel for a step-like switching of $V_D \to 0$ at some points in the device. The dotted lines denote theoretical results calculated with the time constants shown in fig. 12. (b) The time responses of energy and population of the lower vally for the same switching as (a). The responses for the two points with the almost same energy just before the switching are shown together in each figures by the solid and dotted lines.

TRANSPORT EQUATIONS WITH RELAXATION TIMES OF ENERGY AND MOMENTUM

It is not easy, however, to study on accuracy of the relaxation time approximation directly from the transient simulation. In the present work we will simply discuss it from the steady state data of the present work.

It is well known that Blotekjaer(1970) derived transport equations for description of near ballistic transports in GaAs, and Cook and Frey(1982) developed a tractable set of the equations. Their equations are written in steady state as follows.

$$\mathrm{(1)} \qquad \mathbb{v} = \tau_p \left[e\mathbb{F} - \nabla(2\mathcal{E}/3) - (2\mathcal{E}/3n)\nabla n \right] / m^*$$

$$\mathrm{(2)} \qquad \mathbb{v} \cdot \nabla(5\mathcal{E}/3) = e\mathbb{v}\cdot\mathbb{F} - (\mathcal{E} - \mathcal{E}_0)/\tau_\mathcal{E}$$

Here the notations have usual meanings. The equations were derived with the assumptions of the displaced Maxwellian distributions and of neglecting the kinetic energy of electron drift compared with the thermal kinetic energy. Naturally the latter assumption is valid near the source and drain sides away from the gate. The contribution of the kinetic energy of electron drift to the total energy, however, reaches about 20 % under the gate in the ON state described in the former sections due to the near ballistic transports.

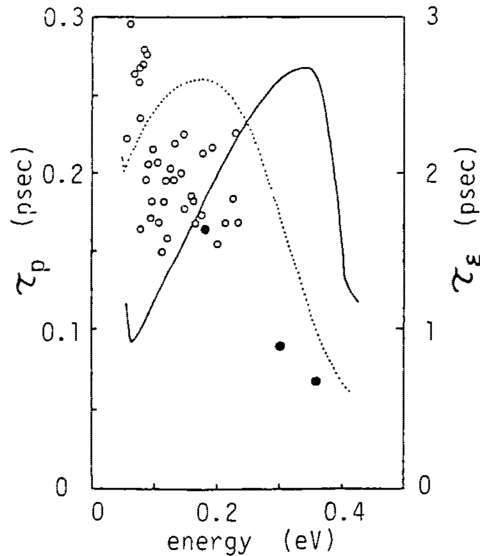

Fig. 12. The relaxation times of energy and momentum and the time constants evaluated from the time responses of energy and momentum. The solid and dotted lines denote τ_ε and τ_p obtained from steady state data in an ensemble Monte Carlo simulation for an uniform electric field case. The open and closed circles show the time constants of energy and momentum evaluated from their time responses by the simulation, respectively.

Using the equations and noticing the boundary conditions for particle dynamics, let us evaluate τ_ε and τ_p from the ON steady state through Eqs. (1) and (2).

First we have evaluated τ_ε and τ_p from the data on the drain side of the peak of energy. Although the values of τ_ε are fairly scattered , they are in good agreement with the solid line in fig. 12 in the range of $0 < \varepsilon < 0.4$ eV. On the other hand, the values of τ_p are considerably small in comparison with the dotted line. It is considered that the small values is due to the thermal equilibrium condition in the drain electrode. Thus, the influence of the drain electrode on τ_ε is small, but it on τ_p extends inside.

The situation changes drastically in the source side of the peak of energy, namely under the gate. Figure 13 shows the values of α_ε and α_p which are defined by $\alpha_\varepsilon = 1-(5/3)\mathbf{w}\cdot\nabla\varepsilon/\mathbf{w}\cdot\mathbb{F}$ and $\alpha_p = 1-(2/3)[\partial\varepsilon/\partial z + (\varepsilon/n)\partial n/\partial z]/qF_z$, respectively. Then τ_ε and τ_p are written by $(\varepsilon-\varepsilon_0)/(q\mathbf{w}\cdot\mathbb{F}\,\alpha_\varepsilon)$ and $m^*v_z/(qF_z\,\alpha_p)$. It is obvious that their negative values in fig. 13 are physically meaningless. This means that Eqs. (1) and (2) may underestimate ε and overestimate $\mathbf{w}$ under the gate compared with the multi-particle simulation. As the results, Eqs. (1) and (2) may overestimate the drain current. It is considered that the negative values of α_ε and α_p are caused by the assumptions

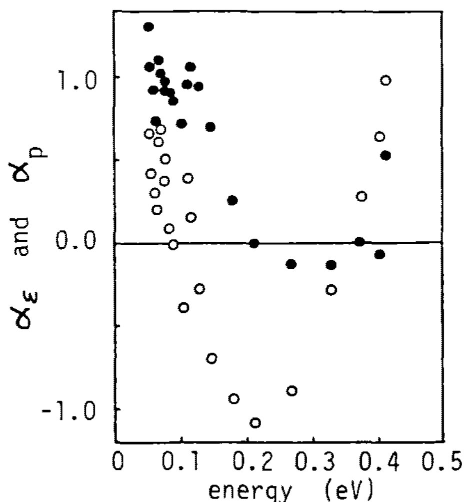

Fig. 13. The energy dependences of α_ε(○) and α_p(●).

in the equations. Thus, the equations are not valid or less accurate under the gate where the near ballistic transport is significant.

A way to simply improve numerical results on the distribution of energy is to use a modified value of τ_ε larger than the original one. The use may make up for the invalid assumptions in Eqs. (1) and (2). The influence of the thermal equilibrium in the drain electrode on the momentum indicates that careless movement of the drain electrode toward the gate, which may be useful for reduction of the number of the particles employed in the simulation, make the average velocity of particles small in the drain side.

DISCUSSION AND CONCLUSIONS

We have presented the time-resolved distributions of energy, velocity, electric-field and carrier density during the ON → OFF switchings, using the multi-particle simulator which self-consistently simulates the particle dynamics and the electric-field. In particular we have depicted the near ballistic transports proper to the ON → OFF switchings. In the initial period of the switchings less than 1 psec, the near ballistic transports of the particles in the lower valley are temporary caused by the large local field. The velocities exceed the maximum velocity in the DC operation. In the OFF → ON switching there are two kinds of the near ballistic transports at the source and under the gate. The slow responses after the period are caused by the particles in the upper valleys. Consequently, the over-all switching-time is strongly dependent on how many particles there are in the upper valleys.

We have also presented the time-resolved data on the relaxation process. The carrier density and momentum quickly

relax within about 0.7 psec, while the energy relaxes very slowly. In the initial period of the relaxation the particles in the lower valley near the drain move ballistically.

Thus, we have shown that the multi-particle simulator is a useful tool for investigation of features of electron dynamics and device performance in the switching operation. It has been found from evaluation of the relaxation times that Eqs. (1) and (2) are less accurate for description of the near ballistic transport under the gate. They underestimate the energy and overestimate the velocity. The drain current may be overestimated by them.

REFERENCES

Blotekjaer K.(1970). Transport Equations for Electrons in Two-Valley Semiconductors. IEEE Trans. Electron Devices, ED-7, pp. 38-47.

Cook R. K. and J. Frey(1982). Two-Dimensional Numerical Simulation of Energy Transport Effects in Si and GaAs MESFET's. IEEE Trans. Electron Devices, ED-29, pp.970-977.

Fawcett W., A. D. Boardman and S. Swain(1970). Monte Carlo Determination of Electron Transport properties in Gallium Arsenide. J. Phys. Chem. Solids, 31, pp. 1963-1990.

Yokoyama K., M. Tomizawa and A. Yoshii(1985). Scaled Performance for Submicron GaAs MESFETs. IEEE Trans. Electron Device Letters, EDL-6, pp. 536-538.

Yoshii A, M. Tomizawa and K. Yokoyama(1983). Accurate Modelling for Submicrometer-gate GaAs MESFET's Using Two-dimensional Particle Simulation. IEEE Trans. Electron Devices, ED-30, pp. 1376-1380.

Stenzel R., H. Elschner and R. Spallek(1987). Numerical Simulation of GaAs MESFETs Including Velocity Overshoot. Solid-State Electronics, 30, pp.873-877.